NUCLEAR SCIENCE AND ENGINEERING: **155**, 395–408 (2007)

High-Fidelity Light Water Reactor Analysis with the Numerical Nuclear Reactor

David P. Weber, Tanju Sofu, and Won Sik Yang

Argonne National Laboratory, 9700 South Cass Avenue, Argonne, Illinois 60439

Thomas J. Downar, Justin W. Thomas, and Zhaopeng Zhong

Purdue University, 1290 Nuclear Engineering, West Lafayette, Indiana 47907-1290

Jin Young Cho, Kang Seog Kim, and Tae Hyun Chun

Korea Atomic Energy Research Institute
150 Dukjin-dong, Daejeon 305-600, Korea

and

Han Gyu Joo* and Chang Hyo Kim

Seoul National University, San 56-1, Sillim-dong, Seoul 151-742, Korea

Received January 31, 2006
Accepted May 18, 2006

Abstract—*The Numerical Nuclear Reactor (NNR) was developed to provide a high-fidelity tool for light water reactor analysis based on first-principles models. High fidelity is accomplished by integrating full physics, highly refined solution modules for the coupled neutronic and thermal-hydraulic phenomena. Each solution module employs methods and models that are formulated faithfully to the first principles governing the physics, real geometry, and constituents. Specifically, the critical analysis elements that are incorporated in the coupled code capability are a direct whole-core neutron transport solution and an ultra-fine-mesh computational fluid dynamics / heat transfer solution, each obtained with explicit (sub-fuel-pin-cell level) heterogeneous representations of the components of the core. The considerable computational resources required for such highly refined modeling are addressed by using massively parallel computers, which together with the coupled codes constitute the NNR. To establish confidence in the NNR methodology, verification and validation of the solution modules have been performed and are continuing for both the neutronic module and the thermal-hydraulic module for single-phase and two-phase boiling conditions under prototypical pressurized water reactor and boiling water reactor conditions. This paper describes the features of the NNR and validation of each module and provides the results of several coupled code calculations.*

I. INTRODUCTION

Design and analysis of reactor cores and nuclear power plants have relied heavily on modeling and simulation of key phenomenology, component and system behavior, and the availability of advanced computing systems. Sophisticated models of individual and coupled phenomena, such as neutron transport, thermal hydraulics and heat transfer, structural and thermomechanics, and fuel behavior, have been developed to understand and predict the behavior of the reactor core and its components under steady-state and transient conditions, representing normal, off-normal, and accident conditions. The level of modeling sophistication in routine design and analysis has increased substantially because of improved understanding of the governing physical principles and the availability of advanced computing systems to perform the analyses. Recent developments in

*E-mail: joohan@snu.ac.kr

computing capability, including the development of massively parallel computing systems, now enable not only sophisticated phenomenological modeling but also the application of such high-fidelity models in an integrated analytical environment.

In recognition of these developments, a project was initiated under sponsorship of the International Nuclear Energy Research Initiative (I-NERI) to develop a high-fidelity, integrated core design and analysis tool based on first-principles models, which takes advantage of advanced parallel computing systems. Developed by colleagues at Argonne National Laboratory (ANL), Korea Atomic Energy Research Institute (KAERI), Purdue University, and Seoul National University, this analysis system is referred to as the Numerical Nuclear Reactor[1–4] (NNR). Originally developed for the analysis of pressurized water reactors (PWRs), it has recently been extended to treat boiling water reactors (BWRs). Although the NNR is a computationally intensive analysis system, requiring the use of parallel and massively parallel computing systems, it provides a robust complement to existing design and analysis methodologies. Because it is based on first-principles models being validated against experimental and analytical data, it can serve as an effective benchmark for existing methods and can provide a basis for investigation of phenomena and behavior requiring detailed understanding of coupled phenomena that may not be possible with existing methods.

The traditional approach for analyzing reactor cores involves the separate evaluation of the different phenomenological effects in the system. In this approach, which is still generally widespread at nuclear vendors and utilities, different technical groups perform the neutronic, thermal-hydraulic, and thermomechanical calculations, using information supplied by the other groups. This approach often requires iterations of data between the groups, which can make the process tedious and time-consuming. In this traditional approach, it is generally attempted to loosely couple the different disciplines by defining conservative safety parameter limits that have to be met by the various groups. Obviously, this approach could be very costly if the limits are either too conservative or not conservative enough.

In the neutronic and thermal-hydraulic analysis performed by each group, simplifications and approximations of the system are generally introduced because the direct solution of the basic governing equations can be prohibitive because of computing resource limitations. For instance, approximations such as homogenization, energy group condensation, and neutron diffusion are generally used in the neutronic calculations, whereas one-dimensional flow formulations with numerous experimental correlations are used in the thermal-hydraulic analysis. The separate evaluation of the coupled phenomena with approximate models not only introduces inevitable errors but also lacks the details of the solution. The NNR is designed to provide high-fidelity solutions in reactor core analysis by integrating first-principles–based simulation models in each phenomenological area.

The critical analysis elements that are incorporated in the coupled code capability are a direct whole-core neutron transport solution and an ultra-fine-mesh computational fluid-dynamics (CFD) / heat transfer solution, each obtained with explicit (sub-fuel-pin-cell-level) heterogeneous representations of the components of the core. The considerable computational resources required for such highly refined modeling are addressed by using massively parallel computers, which together with the coupled codes constitute the NNR. Modeling parameters can also be relaxed in the NNR to make practical applications tractable on clusters of workstations and personal computers but with the assurance that the more rigorous model is available to evaluate consistently the errors introduced by the reduced-order model.

The development of the NNR involved a significant amount of developmental and modeling effort. First, a direct whole-core neutronic calculation code, Deterministic Core Analysis based on Ray Tracing (DeCART) code, was developed, which is capable of direct three-dimensional (3-D) transport calculation for PWRs at power-generating conditions. A coupling methodology was then developed and implemented to couple the CFD calculation with the whole-core neutronic calculation. The project also included extensive verification and validation of the individual modules of the NNR. Results from the reactor physics area showed DeCART to be very accurate in comparison to a range of high-fidelity Monte Carlo simulations and experimental measurements. CFD results for single-phase flow were found adequate in comparison to experimental results, and best-practice guidelines for turbulence modeling were identified. The NNR was also extended to handle two-phase-flow systems because of interest in detailed understanding of integrated neutronic and thermal-hydraulic conditions in BWRs. Extension of the DeCART methodology to treat the more complex geometry of the BWR fuel assembly was performed, and a series of verification and validation activities was initiated. In order to treat two-phase boiling conditions in PWRs and BWRs, new models, which are also undergoing extensive verification and validation, were developed and implemented in the CFD code used in the NNR. In Secs. II and III, the development and validation of the neutronic and CFD-based thermal-hydraulic modules are described. The code coupling methodology and demonstrative coupled calculation results are then provided in Sec. IV. Section V concludes the paper with continuing work and future applications of the NNR.

II. THE DECART DIRECT WHOLE-CORE TRANSPORT CALCULATION CODE

The current practice in light water reactor (LWR) core analysis is to use pregenerated homogenized few-group

constants to obtain the whole-core power distribution and reactivity. One objective of the research here was to remove this limitation and consequently the errors associated with a priori spatial homogenization and group condensation. The DeCART code[5] was developed for the direct whole-core neutronic calculation and is capable of generating the 3-D sub-pin-level power distribution with the thermal feedback effect directly incorporated. The term "direct" is used loosely here to reflect the fact that the core calculation can be performed directly, once a multigroup (e.g., 45 or more groups) cross-section library for the thermal reactors is available. A direct whole-core transport calculation for practical 3-D problems can be computationally prohibitive, and therefore, various innovative methods are used in the DeCART solution to reduce the computational burden such as the planar method of characteristics (MOC) solution-based coarse mesh finite difference (CMFD) scheme and multiprocessing.

The planar MOC solution–based scheme takes advantage of the fact that the primary heterogeneity in the LWR occurs in the radial plane. The two-dimensional (2-D) MOC calculation[6] is performed in each plane of the 3-D domain to generate pin-cell homogenized, equivalent multigroup cross sections that are then used in a 3-D CMFD calculation.[7] Prior to the transport calculation, however, the self-shielded multigroup cross sections are determined, which are composition, geometry, and temperature dependent. This is carried out by using the subgroup method that was formulated suitably for the dynamic generation of multigroup cross sections in the resonance region at nonuniform temperature conditions. The planar MOC solution–based CMFD method and the temperature-dependent subgroup method are the two primary calculation methods of DeCART for the direct whole-core solution. These two methods and some of the validation of the methods are described in Secs. II.A and II.B.

II.A. Direct Three-Dimensional Whole-Core Calculation Methodology

For the direct whole-core calculation, local heterogeneity at the sub-pin level should be explicitly represented. MOC is an effective transport solution method for such highly refined heterogeneous problems, and numerous MOC-based whole cores such as CASMO-4E (Ref. 8) have been developed and successfully applied to LWR problems. The 3-D MOC calculation for the whole reactor problem is, however, computationally unrealistic even with today's high-performance computers since it would require a prohibitive number of neutron ray tracings. Therefore, an approximate 3-D transport solution method involving 2-D planar MOC solutions was devised for practical calculations based on the following rationale.[9] Since most heterogeneity in a reactor problem appears in the radial direction rather than in the axial direction, it is sufficient to apply the MOC to resolve only the radial dependency and to use a lower-order method for the axial direction.

In this method, the 2-D planar MOC solutions are iteratively combined with pin-cell–based 3-D CMFD solutions. The planar MOC solution provides the CMFD problem with cell-homogenized group constants and also the radial coupling coefficients that relate the interface current with two node average fluxes. The cell homogenization is performed during the calculation so that no a priori homogenization is necessary.[10] Pin-cell–sized nodes are employed radially in the CMFD formulation while much larger nodes with sizes up to 20 cm are used axially. The axial dependence of the flux within the large node can be described by a lower-order method, namely, the nodal expansion method[11] with the diffusion approximation. It should be noted that this lower-order axial treatment can potentially deteriorate the solution accuracy when there is a severe axial heterogeneity. The planar MOC problems are developed consistently with the global 3-D CMFD problem in order to preserve the neutron balance. This is accomplished by introducing an axial leakage source into the planar MOC calculation at each pin cell that is determined from the CMFD solution. Another important function of the CMFD solution is to accelerate the source convergence of the MOC calculation.[12] In the following section, the essential ideas of this method are presented, but a more detailed description can be found in the references.[13]

For a 3-D neutron transport problem in which several radial planes are used, a transverse integration can be used to treat the axial neutron leakage as a source term in the planar neutron balance equation. As is normally done in the transverse-integrated nodal methods, the transport equation for a discretized angle m can be integrated over the axial direction on a plane (designated by plane index k) to yield

$$\left(\varepsilon_m \frac{\partial}{\partial x} + \eta_m \frac{\partial}{\partial y}\right) \bar{\varphi}_m^k(x,y) + \Sigma_t^k(x,y)\bar{\varphi}_m^k(x,y) = \bar{Q}_m^k(x,y) - L_{z,k}^m(x,y) \ , \quad (1)$$

where

$\bar{\varphi}_m^k(x,y)$ = axially averaged angular flux

$\bar{Q}_m^k(x,y)$ = axially averaged neutron source consisting of fission and scattering sources

$L_{z,k}^m(x,y)$ = axial leakage source representing the axial gradient in the angular flux distribution.

Since the axial leakage term is generally much smaller than the neutron fission and scattering sources, it is plausible to introduce an approximation to the angular and spatial dependence of this term. Specifically, the approximate axial leakage term can be constructed iteratively

by using the surface average net current and flux determined at the axial interface from the 3-D CMFD calculation.

Once the axial leakage source term is determined, Eq. (1) can be solved by a 2-D ray-tracing scheme. In DeCART, a pin-cell–based modular ray-tracing (CMRT) scheme was originally implemented. The pin-cell–based method considerably reduces the memory requirements by storing the ray segment information only for typical cells, which is possible by suitably choosing the azimuthal angle and ray spacing such that the same ray pattern can be repeated in all the pin cells. The CMRT has, however, limited applicability. For example, the complex geometry of a BWR cannot be described as a repeating array of pin cells. Therefore, the modular ray-tracing scheme in DeCART was generalized by adding an assembly-based modular ray-tracing [Assembly Modular Ray Tracing (AMRT)] method. With AMRT, the association of ray segments with flat source regions is determined in two stages. The assembly module is divided into rectangular cells aligned in a regular array; these rectangular cells provide the basis for the CMFD mesh. Each cell is further divided into flat source regions with a more complex geometry, which is the mesh unit for the MOC calculation.

The solution of the 2-D MOC problem determines the scalar flux at each region within a pin cell and also the net current at the cell surfaces. These intracell scalar flux distributions can be used to define the cell average cross sections while the cell surface current is used to define the radial coupling coefficients that express the interface current as a function of the two adjacent node average fluxes. Unlike the radial coupling relations, the axial coupling relations are determined within the 3-D CMFD formulation. They are established by using the partial current scheme of the nodal expansion method, which expresses the outgoing current at a surface in terms of the two incoming currents, the node average flux, and two source moments. The source moments here include the contributions from the quadratic radial transverse leakage terms. The radial and axial coupling relations yield the following CMFD nodal balance equation expressed in terms of the node average fluxes, the incoming partial currents, and the axial flux moments as

$$
\begin{aligned}
&-\frac{1}{h}\sum_{s=1}^{N_{rad}^{i}}(\tilde{D}^{i,s}+\hat{D}^{i,s})\bar{\phi}^{i,s}\\
&\quad+\left\{\Sigma_r^i+\frac{2T_3^i}{h_z}+\frac{1}{h}\sum_{s=1}^{N_{rad}^{i}}(\tilde{D}^{i,s}-\hat{D}^{i,s})\right\}\bar{\phi}^{i}\\
&\quad=\bar{S}^i-\frac{1}{h_z}(T_1^i+T_2^i-1)(J_z^{-i,T}+J_z^{-i,B})-\frac{2T_5^i}{h_z}\tilde{\phi}_2^i\ ,
\end{aligned}
\tag{2}
$$

where

N_{rad}^i = number of radial neighboring nodes of node i

$\tilde{D}^{i,s}, \hat{D}^{i,s}$ = radial coupling coefficients determined from the MOC solution

$T_m^{i,s}$ = coefficients needed for the axial outgoing current relation

$J_z^{-i,T}, J_z^{-i,B}$ = incoming currents at the top and bottom surfaces, respectively

$\tilde{\phi}_2^i$ = second-order moment

$\bar{S}^i$ = source including the fission and the scattering.

The incoming currents and the second moments on the right side are assumed to be available from the previous iteration so that Eq. (2) becomes essentially a 2-D problem. The axial incoming currents are updated by the plane sweep to solve the 3-D problem.

The MOC and CMFD problems represented by Eqs. (1) and (2) are coupled with each other. The MOC solution provides the CMFD problem with the cell homogenized cross sections and the radial coupling coefficients whereas the CMFD solution provides the MOC problem with the cell average fluxes and axial leakages. The cell average flux is used to adjust the regionwise fission and scattering source in the MOC calculation. These two calculations are thus performed alternately until the coupled solution converges.

The transport solution process outlined above is carried out using the self-shielded multigroup cross sections determined for each region by the subgroup method, in which the effective cross section of a resonance isotope (represented by R below) for an energy group (denoted by g) is expressed with the following quadrature formula:

$$
\bar{\sigma}_{ag}^{R}=\frac{\sum_i w_i\,\phi_i\,\sigma_{ai}^{R}}{\sum_i w_i\,\phi_i}\ , \tag{3}
$$

where σ_{ai}^R, w_i, and ϕ_i are the subgroup level, weight, and flux, respectively, corresponding to the i'th subgroup. In order to apply the above formula, the flux of each subgroup level needs to be determined for each resonance region. The method for determining the fluxes involves the solution of the so-called subgroup fixed source problem, which can be written as

$$
\begin{aligned}
&\Omega\cdot\nabla\varphi(\mathbf{r},\Omega)+(N_R(\mathbf{r})\sigma_m+\lambda\Sigma_p(\mathbf{r}))\varphi(\mathbf{r},\Omega)\\
&\quad=\frac{1}{4\pi}\,\lambda\Sigma_p(\mathbf{r})\ ,
\end{aligned}
\tag{4}
$$

where

N_R = number density of the resonance absorber

σ_m = prespecified m'th subgroup level

λ = hydrogen equivalence factor.

Equation (4) is solved for the angular flux distribution of a subgroup using the isotropic slowing-down source determined under the assumption that the scalar flux above the resonance group of interest is unity throughout the core. In this problem, the same subgroup level σ_m is used everywhere, signifying that the neutrons belonging to the subgroup would experience the same absorption cross section regardless of their energy or position. This is reasonably valid under a uniform temperature condition since a neutron that survived from collision in one region would leave the region with the same energy, and thus, its subgroup will not be changed. The cross section it would experience in the next region will be the same as in the region it left. In the case of nonuniform temperature distributions, an approximate method was developed in which the subgroup levels are adjusted according to temperature-dependent subgroup weights.[14]

Equation (4) can be solved by employing the same transport solver used for the regular transport solution of the whole-core problem. In the case of DeCART, the MOC solver is used to determine the angular and subsequent scalar flux distribution. Once the scalar flux is obtained for each region, equivalence between the heterogeneous and the homogeneous systems is imposed to represent the solution flux with the formula for the homogeneous cases. In order to consider resonance interactions between different isotopes, the resulting background equivalence cross section is functionalized over the subgroup level similar to the method used in the HELIOS code.[15]

II.B. Solution Verification and Validation

The DeCART code was validated using a series of benchmark problems to assess the accuracy of various approximations in the calculation, as well as the accuracy of the overall solution methodology. The first benchmark problem involved heterogeneous core configurations with given cross sections. As reported in previous papers,[9,13] the DeCART solution accuracy is excellent for both the original and rodded C5G7MOX benchmark problems. The eigenvalue error is <200 pcm, and the pin-power error is $<2\%$ even for the rodded cases involving severe axial heterogeneity. This demonstrates that the degradation in the accuracy attributable to the low-order method used for the axial treatment is not very significant.

More practical and extensive verifications were then performed primarily by comparing DeCART and continuous-energy Monte Carlo solutions. This was done by solving a series of test problems by both codes that spans a wide range of geometrical configurations and temperature conditions. The DeCART and Monte Carlo models used the same modeling parameters such as isotopic number densities and temperatures. Specifically, the regionwise temperature distribution determined by the DeCART calculation was used in the corresponding Monte Carlo calculation so that the identical temperature distribution was used in both cases.

The first set of test problems was used to assess the accuracy for PWR applications and was based on a typical 17×17 PWR fuel design. For the PWR cases, comparisons were made between DeCART and the MCCARD Monte Carlo code.[16] The fuel rod consists of 4.95 wt% UO_2 pellets and Zr cladding whose diameters are 0.805 and 0.952 cm, respectively. The isotopic number densities of the fuel, cladding, and coolant are specified so that both codes use the same composition. The active core height is 2 m. The geometrical configurations of the test problems consist of pin cell, assembly, and two minicores in both two and three dimensions. The basic minicore (case A) consists of 21 identical fuel assemblies (four corner assemblies removed from the 5×5 fuel assembly lattice), and the other (case B) has a checkerboard-type arrangement of 4.95 and 2 wt% fuel assemblies. Both uniform temperature conditions representing the hot-zero-power condition and nonuniform temperature conditions representing the hot-full-power (HFP) and the hot-double-power (HDP) conditions are specified. The HDP condition is added to compensate for the low power density of the HFP case. A 47-group cross-section library was used in the DeCART runs while the continuous-energy cross sections generated with a 10 K interval from 300 to 2500 K were used in MCCARD.

The reactivity obtained by DeCART and MCCARD for the pin cell (PC), fuel assembly (FA), and minicore (MC) are compared in Table I. The full-power (F) and the double-power (D) cases involve nonuniform fuel temperatures while the hot 600 K (H) and the zero power cases are the uniform temperature cases. In the MCCARD runs, sufficient neutron histories were used to yield standard deviations of the reactivity <10 pcm. For the PC and FA cases, the reactivity difference between the two codes is <70 pcm for the four temperature conditions examined. There are various factors affecting the accuracy of a deterministic transport code such as the transport solver, basic cross-section data, and the resonance self-shielding treatment method. The good agreement between the DeCART and MCCARD reactivity implies that the DeCART method and data, particularly the resonance treatment method and data, are sufficiently accurate. The error in the reactivity becomes larger for the minicore case where there is large radial leakage. However, even in these cases the difference is <200 pcm, which still represents a reasonable accuracy.

The power-generating minicore cases involve highly nonuniform fuel temperature distributions since the power vanishes at both radial and axial boundaries. Therefore, it should be a good measure of the effectiveness of the

TABLE I

Comparison of k_{eff} for Different Temperature Profiles

Configuration	Code	H (600 K)	Z (543 K)	F (100%)	D (200%)
PC					
2D	DeCART	1.40342	1.43914	1.42052	1.41385
	MCCARD	1.40220	1.43880	1.41975	1.41347
	Difference, pcm	62	16	38	19
3D	DeCART	1.38212	1.42110	1.39847	1.39003
	MCCARD	1.38147	1.42134	1.39867	1.39024
	Difference, pcm	34	−12	−10	−11
FA					
2D	DeCART	1.43057	1.46181	1.44521	1.43897
	MCCARD	1.43012	1.46201	1.44540	1.43914
	Difference, pcm	22	−9	−9	−8
3D	DeCART	1.40868	1.44349	1.42299	1.41507
	MCCARD	1.40913	1.44458	1.42396	1.41623
	Difference, pcm	−23	−52	−48	−58
MC					
2D-A	DeCART		1.36700	1.34212	1.33513
	MCCARD		1.36455	1.33945	1.33266
	Difference, pcm		131	149	139
2D-B	DeCART		1.28388	1.26135	1.25470
	MCCARD		1.28082	1.25820	1.25155
	Difference, pcm		186	198	201
3D-A	DeCART		1.35027	1.31977	1.31106
	MCCARD		1.34891	1.31813	1.30920
	Difference, pcm		75	94	108
3D-B	DeCART			1.23995	
	MCCARD			1.23757	
	Difference, pcm			155	

subgroup method implementation for nonuniform temperature cases. The radial power distribution error of DeCART for the checkerboard-type loading minicore case (case B) is shown in Fig. 1. As can be seen in Fig. 1, the pin-power error is $<0.7\%$, and no particular trend is observed. This extent of the agreement is noted in other minicore cases as well, as can be identified in the power distribution comparison summary given in Table II.

The second set of cases was used to verify the AMRT method in DeCART. It consists of three 2-D test problems involving two types of BWR assemblies. The first assembly type is modeled after a UO_2 Atrium10 assembly mentioned in an Organization for Economic Cooperation and Development/Nuclear Energy Agency (OECD/NEA) benchmark,[17] and the other is similar to a GE10 assembly (an artificial design). The first two problems are single-assembly problems for each fuel type while the third problem is a 2×2 checkerboard-type problem consisting of these two assembly types. The fuel rod array of the Atrium10 assembly is 10×10 while that of the GE10 assembly is 8×8.

The reference solutions for these problems were obtained by MCU Monte Carlo simulations.[18] The standard deviation in the MCU simulations was 20 pcm in all cases. The error in the eigenvalue and pin-power distribution of the DeCART solutions is summarized in

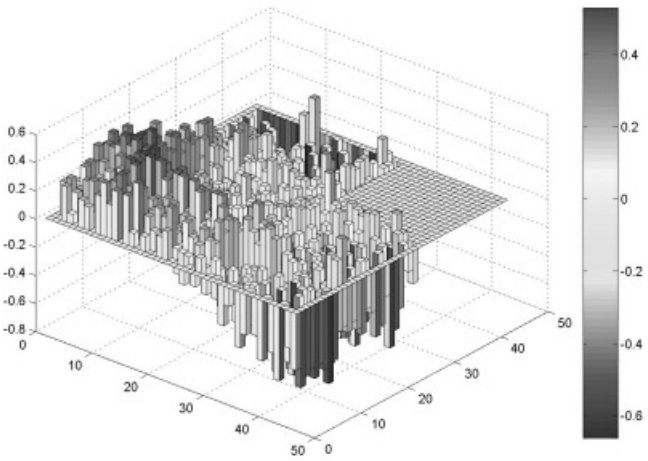

Fig. 1. Radial pin-power error of DeCART [DeCART-MCCARD (%)].

TABLE II

Summary of Power Distribution Errors for the Minicore Cases

Case	Axially Averaged					Three-Dimensional-Wise		
	Root-Mean-Square Error (%)	Maximum Error (%)		Fr		Root-Mean-Square Error (%)	Maximum Error (%)	
		Absolute	Relative	Value	Error (%)		Absolute	Relative
MC3Z-A	0.15	0.63	0.50	1.825	0.04	0.45	2.11	3.42
MC3F-A	0.23	0.82	0.69	1.671	0.10	1.77	5.27	6.97
MC3D-A	0.33	1.26	0.84	1.650	0.15	1.60	4.89	6.36
MC3F-B	0.26	0.92	0.67	1.922	0.12	1.43	4.58	6.08

TABLE III

Comparison Summary for the 2-D BWR Assembly Cases

Model	MCU k_{eff}	Error in k_{eff} (pcm)	Root-Mean-Square Pin Power Error (%)	Maximum Pin Power Error (%)
Atrium10	1.1033	105	0.77	1.99
GE10	1.0979	−96	0.98	2.07
Checkerboard	1.1010	1	0.85	2.01

Table III, and the pin-power error of the fine-mesh checkerboard case is shown in Fig. 2. Since the eigenvalue error is ~110 pcm and the pin-power error is 2% in the fine-mesh cases, these results provide confidence in the accuracy of the ARMT module in DeCART.

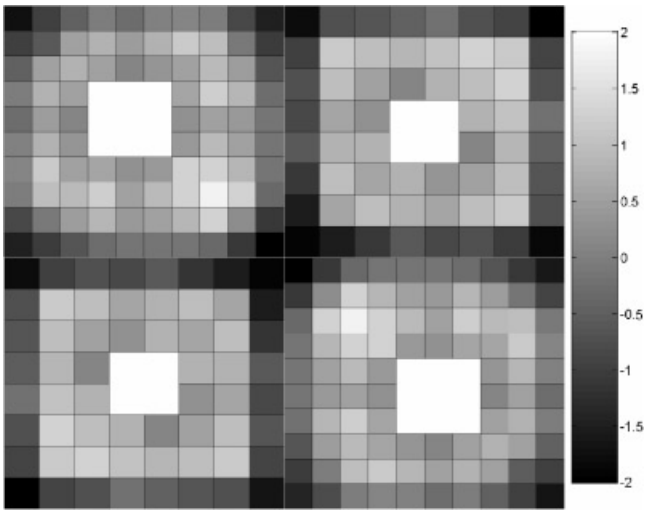

Fig. 2. DeCART pin-power error (%) for the 2×2 checkerboard problem (fine angular discretization).

For the Atrium10 model, additional comparisons were made for the intra-pin-power distribution in a few selected pins. The results compare 12 regions within the fuel pellet, with 3 radial divisions and 4 azimuthal divisions, as shown in Fig. 3. These results are compared with those of MCU in Table IV for a sample pin. This sample pin is adjacent to a water channel on one side. Table IV gives the relative power in each division obtained from the MCU simulation and the relative error (in parentheses) in the DeCART prediction. The maximum error is <1.25%. The standard deviation in the Monte Carlo calculation was between 0.4 and 0.6%.

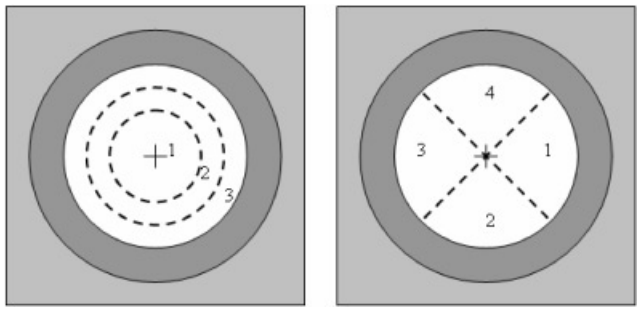

Fig. 3. Pin edits regions for DeCART and Monte Carlo power distribution.

TABLE IV

Comparison of Monte Carlo and DeCART Intra-Pin-Power Distribution

Azimuthal Division	Radial Division		
	1	2	3
1	0.99 (−0.06%)	1.07 (−0.59%)	1.14 (−0.95%)
2	0.96 (0.60%)	1.00 (1.23%)	1.06 (0.21%)
3	0.93 (0.55%)	0.95 (−0.05%)	0.98 (−0.62%)
4	0.95 (−0.32%)	0.97 (−0.13%)	1.01 (0.06%)

III. COMPUTATIONAL FLUID DYNAMICS FOR CORE THERMAL-HYDRAULIC ANALYSIS

With the advance of parallel computers and their wider availability, the analysis of thermal-hydraulic phenomena in a reactor core based on solutions of the Navier-Stokes equations is gaining acceptance by the reactor design community.[19,20] A highly refined CFD model with the ability to resolve the effects of spacer grid on thermal mixing and cross flow has the potential to dramatically improve the accuracy of core design. As part of the NNR development effort, the CFD methods were used to calculate the flow and heat transfer using a rigorous pin-by-pin representation of fuel assemblies and surrounding coolant channels in the core.[1] Using fine-mesh CFD solutions in each coolant channel offers an integrated whole-core analysis capability to capture important feedback effects between the first-principles–based models.

Many widely used CFD software codes were considered, and their specific capabilities relevant to the integrated simulation of a reactor core were reviewed. These capabilities include turbulent flow and heat transfer simulations, conjugate heat transfer between the fluid and solid regions, steady-state and transient analyses, single-phase and multiphase flow, moving boundary and deforming mesh structures, fluid-structure interactions, and efficient parallel computing schemes. More detailed evaluations were performed with STAR-CD and the CFD-ACE codes, primarily because of their availability at ANL and KAERI, respectively.

The commonly used turbulence models were evaluated for the prediction of flow and heat transfer in various rod-bundle configurations. Solving the Navier-Stokes momentum equations in conjunction with the continuity and energy conservation equations to simulate flow and heat transfer in a reactor core (including the fluid and solid domains) offers a mechanistic approach based on first principles. Because of the scale of the problem, however, the field variables and Reynolds stresses are often expressed in terms of their ensemble averages that are linked to the mean flow field via turbulence closure models. These closure models consist of a set of additional differential or algebraic equations. The most commonly used turbulence models fall under the category of Reynolds Averaged Navier-Stokes (RANS) models. The standard k-ε model is based on the linear eddy viscosity hypothesis for the Reynolds stresses.[21–23] The anisotropic eddy viscosity relationship removes the assumption of turbulence isotropy by using quadratic[24–26] and cubic[27] constitutive formulations for the stress-strain relations. Other variations of RANS models include the renormalization group version[28] and Chen's variant.[29] The more complex second-order closure models such as the differential Reynolds Stress Model (RSM) are based on exact transport equations for the individual Reynolds stresses as derived from the Navier-Stokes equations.[30]

The RANS-based turbulence models were first assessed for heat transfer in a pipe (with an equivalent hydraulic diameter of a typical PWR flow channel) and compared to the values predicted with the well-known Dittus-Boelter[31] correlation. For Re numbers ranging from 25 000 to 500 000 corresponding to PWR operating conditions from 5% to full power, the heat transfer coefficients computed at the wall by most RANS models were generally within the experimental uncertainty of the correlation ($\pm 10\%$). The predictions with the two-layer model[23] for Re = 254 809 differed from the correlation only 3.5%, suggesting that the fine-mesh resolution of the boundary layer may result in improvement in heat transfer predictions.

The assessments of turbulence models for single-phase flow were performed for both the bare-rod-bundle configurations and fuel assemblies with spacer grids.[32] The numerical simulation of turbulent flow structure was performed for six-pin square-pitch[33] and a 37-pin triangular-pitch[34] bare-rod-bundle configurations. In both cases, a symmetric subsection of the test subchannel was modeled for a set of pitch-to-diameter ratios. The turbulence-driven secondary flows were captured with all nonlinear RANS and RSM models, exhibiting a lateral recirculation pattern in the subchannel caused by anisotropy in turbulence. In both studies, the CFD predictions were found to be generally in good agreement with the time-averaged experimental velocity and temperature profiles. However, the axial velocity distribution is consistently underpredicted in the narrow gap between the fuel pins and overpredicted in the subchannel center by all turbulence models. The nonlinear k-ε models provide more accurate predictions over the standard k-ε model; however, the best agreement with the experimental results is obtained with the higher-order (and more computation-intensive) RSM.

The radial variations of turbulence intensities show a similar trend with the RSM predictions being in better agreement with the measured values. While the experimental data suggest a significant increase in the azimuthal turbulence in the narrow gap between the fuel pins, the predicted values were considerably lower than the measured ones.[35] The CFD calculations also predicted larger peripheral variations in wall temperature and shear stress compared to ~3% variation observed in experiments. The discrepancy was larger for smaller pitch-to-diameter ratios, revealing the limitation of RANS methods in capturing the large eddy fluctuation between two adjacent rods.

Originally developed for PWRs, the NNR is currently being extended for BWR applications under a program cofunded by the U.S. Department of Energy (DOE) and the Electric Power Research Institute. Implementation and validation of a new Eulerian two-phase-boiling heat transfer model in the fluid dynamics module STAR-CD and its application for prototypic BWR fuel assembly configurations as part of the integrated analysis capabilities of NNR are an ongoing effort.[36]

IV. COUPLED CALCULATIONS

After demonstrating the validity of the individual components of the NNR, the focus of the project was then to demonstrate an integrated analysis capability using the multiphysics models. Several general-purpose coupling schemes were developed, and the solutions were compared as part of the quality-assurance plan. Various iteration strategies for exchange of relevant information among the modules were also investigated in order to examine such modeling options as the mapping between the very different neutronic and thermal-hydraulic grids. The coupling of CFD and MOC in the NNR was very different from conventional LWR coupled codes in which multiple neutronic nodes were generally mapped to a single thermal-hydraulic mesh. In the NNR the mesh size in CFD is much smaller than the neutronic MOC mesh, and there are considerably larger and more complex data transfer requirements.

IV.A. Coupling Methodology

The coupling of DeCART and STAR-CD was achieved using an external interface program.[37,38] The first task that the interface performs is to map the CFD and DeCART meshes. As shown in the pin-cell problem in Fig. 4, the CFD mesh is significantly finer than the DeCART spatial mesh. This difference is even more significant in the axial direction, where a DeCART plane may be divided into 20 to 50 layers of CFD cells. In the NNR, the modeler is required to generate the CFD mesh such that it is a simple refinement of the coarser DeCART mesh. Thus, each CFD cell is assigned to a single DeCART region, and no partial mapping is permitted. The temperature of a particular DeCART region is computed as a simple mass-weighted average of the temperatures of the CFD cells assigned to that region. The power density distribution within a particular DeCART region is approximated to be flat, and thus, all CFD cells assigned to the same DeCART region are given the same value for the power density.

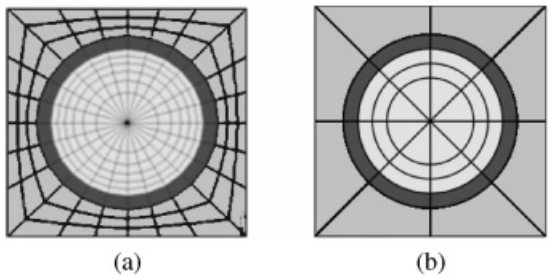

Fig. 4. Schematic showing typical mesh within a fuel pin cell for (a) STAR-CD and (b) DeCART.

The second task performed by the interface is to manage the communication between the CFD and neutronic code modules. The interface serves as the master process with the CFD and neutronic processes as its clients. Each data exchange cycle, STAR-CD transfers the temperature and density of each CFD cell to the interface. The interface then averages these distributions in order to map them to the corresponding DeCART uniform cross-section regions. DeCART then updates its cross sections with the new CFD data. Upon completion of several iterations of the neutron transport calculation, DeCART sends the power density of each flat source region to the interface. This distribution is then reverse mapped to the CFD cells and transferred to STAR-CD. These data exchange cycles continue until calculations are converged, as illustrated in the schematic in Fig. 5.

The amount of data transferred each data exchange cycle can be significant for practical problems. Each data exchange cycle requires the transfer of three CFD cell-wise distributions (temperature, density, and power density). Because the CFD mesh is much finer than the DeCART spatial mesh, the data transfer requirement is governed by the number of CFD cells. For a representative small-core model,[39] there were 64 million cells, and 1.5 gigabytes of data were transferred each cycle. The interface implements a set of customized TCP/IP socket communication functions, which was developed to accomplish communication between the STARCD and DeCART processes, each of which employs its own MPI communicator. The socket communicator has been shown to achieve a transfer speed of 89 megabits/s across compute nodes on the *Jazz* LINUX cluster of ANL on which the coupled calculations were performed. The *Jazz* cluster consists of 350 computing nodes, each of which has a 2.4-GHz Pentium IV CPU with 2 gigabytes of memory.

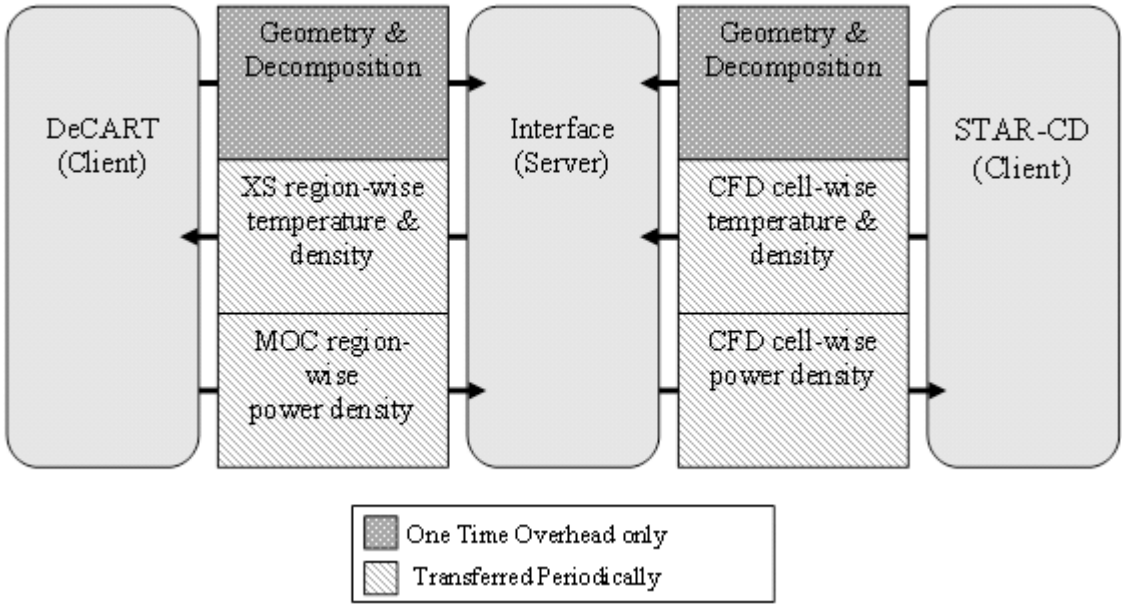

Fig. 5. Schematic of the DeCART/STAR-CD coupling scheme.

The final task for the interface is to monitor and control the convergence of the coupled field solution. The interface monitors the CFD convergence by tracking the enthalpy residual calculated by STAR-CD after each iteration. The enthalpy residual is an indication of how well the temperature distribution has converged based on the most recent DeCART power distribution. Experience has shown that for practical reactor core problems, the enthalpy residual in the fuel is the last to converge. DeCART also computes several residuals after each transport sweep. Typically, these residuals are reduced very quickly, such that it is not necessary to monitor them closely except to ensure final convergence. The interface computes changes in the DeCART regionwise temperature and power distributions from consecutive data exchange cycles. One important convergence criterion is the error in power density distribution:

$$\max_n \left\{ \frac{|q_n^k - q_n^{k-1}|}{q_n^k} \right\} < \varepsilon_q \ , \qquad (5)$$

where q_n^k is the most recently received power density in DeCART flat source region n, and q_n^{k-1} is the previously received power density in the same region. The STAR-CD fuel enthalpy and the power density error criterion are generally the most important indications of coupled calculation convergence.

The procedure for executing a coupled DeCART/STAR-CD calculation can be summarized as follows:

1. The interface computes the mapping of STAR-CD cells onto DeCART regions based on geometry input supplied by each code. The interface then transfers an initial power distribution to STAR-CD.

2. STAR-CD begins iterating using the power distribution supplied by the interface. Once the fuel enthalpy residual is sufficiently small, the CFD cellwise temperature and density distributions are transferred to the interface. STAR-CD waits until the power distribution is updated again. The interface converts the cellwise distribution into a cross-section regionwise distribution and then transfers the data to DeCART.

3. DeCART begins performing transport sweeps using the temperature and density distributions supplied by the interface. Once a prescribed number of transport sweeps have been performed, the power distribution is transferred to the interface. DeCART waits until the temperature and density distributions are updated again. The interface performs the reverse mapping of the power distribution onto the CFD cells and transfers the data to STAR-CD.

4. Evaluate the STAR-CD fuel enthalpy residual and the criterion in Eq. (5). If coupled calculations are not converged, repeat steps 2 and 3.

The completion of steps 2 and 3 comprises the completion of one data exchange cycle. Typically, between 8 and 12 data exchanges are required before the coupled calculations are converged.

IV.B. Coupled Code Convergence Analysis

A convergence study was then performed using the multiassembly checkerboard model to investigate the

effect of data exchange frequency on the coupled calculation convergence. The power density distribution in the CFD calculation is updated after performing N transport sweeps in DeCART, and the density and temperature distributions in DeCART are updated after reducing the fuel enthalpy residual by a factor of α. The purpose of the study was to determine the impact of the values of N and α on convergence of the coupled calculations. The problem was executed on 13 *Jazz* compute nodes, 12 of which were shared by DeCART and STAR-CD, and the interface was executed on the remaining compute node.

As expected, the solution accuracy did not depend on the selection of α and N since the eigenvalues were the same for all cases. It was also observed that the communication time was not a significant contribution to the total run time and was $<2\%$ of the total time. The optimum selection of α and N occurred when the enthalpy and power distributions converged at the same rate. The minimum execution time ($\alpha = 0.05$ and $N = 3$) occurs when the two criteria are satisfied simultaneously. It should be noted that in the cases that showed the best overall performance, the time required for STAR-CD was less than three times the time required for DeCART. The total elapsed time for each case is shown schematically in Fig. 6. The results of this study suggest that the total computation time can be reduced by decreasing the number of CFD iterations and increasing the number of ray tracing sweeps in each data exchange cycle. The results also suggest that the optimum combination of CFD iterations and the number of ray tracings for each data exchange cycle depends on the enthalpy tolerance. This implies that the product of inner and outer iterations (i.e., the total number of enthalpy sweeps) per data exchange cycle is perhaps a more appropriate parameter to track the STAR-CD performance during the coupled calculations.

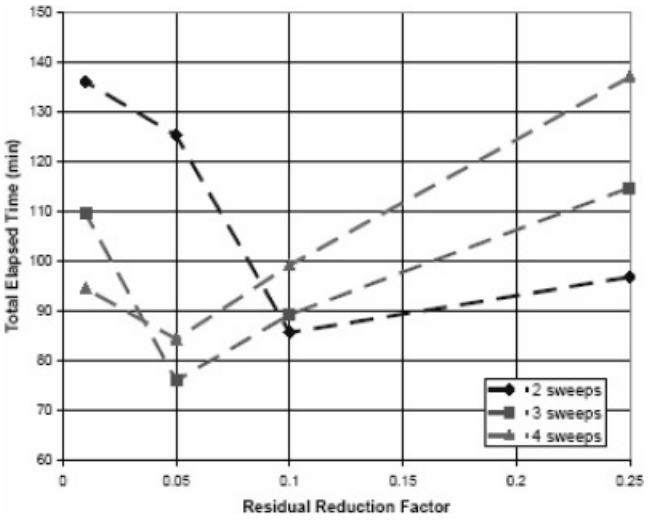

Fig. 6. Total elapsed time as a function of enthalpy residual reduction factor for different numbers of transport sweeps.

IV.C. Coupled Code Application

The practical applications of the NNR focus involve the interaction among the various physical models. Although each of these modules has been developed, verified, and validated for the solution of the individual phenomena, it is the integration and feedback among the fields that provides the ultimate application of interest. Because the original objective of the project was LWR analysis, a testing sequence was developed that included a single-pin model, a multipin model, a fuel assembly model, a multiassembly model, and a small-core model for a typical LWR. Because of space limitations, only the results of the largest problem will be presented here.

A model was developed for a core that is about four times smaller than a typical PWR core. The DeCART model for this problem is a quarter-core with four different types of 17×17 assemblies. The core consists of fuel pins, gadolinium pins, guide tubes, and four types of absorber rods. There are 30 assemblies in the model, 11 of which are radial reflectors. The core configuration is shown in Fig. 7; note that reflector assemblies along the periphery are omitted in Fig. 7. Fuel pins are discretized into three annular rings and eight azimuthal slices. The cladding and moderator each constitute an additional ring per fuel pin, and there are 12 planes in the model including lower and upper plena that function as reflectors. There are approximately $3\frac{1}{2}$ million flat flux zones in the core, and 45 energy groups were used. The angular discretization is such that rays are positioned 0.02 cm apart, and there are eight azimuthal and four polar angles in a 90-deg domain.

The CFD model consists of a one-eighth core segment. There are four axial regions: lower plenum, active

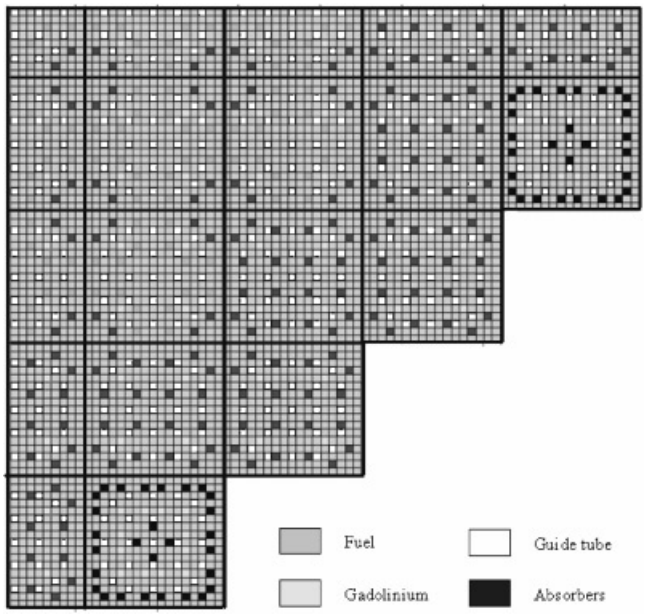

Fig. 7. Pin-by-pin configuration.

fuel, fission gas plenum, and upper plenum. The radial discretization of the fuel pin is similar to DeCART, except that there are two rings in the moderator as shown in Fig. 4. There are 25 azimuthal slices and 200 axial layers in the active part of the fuel pin. This discretization yields more than 64 million cells.

The coupled code calculations were performed on 70 processors of the ANL *Jazz* Linux cluster: 57 for STAR-CD, 12 for DeCART, and 1 for the interface. Steady-state calculations required ~11 h, but no effort has yet been made to optimize the performance. The eigenvalue for this problem was 1.02017, and the pin average fuel temperature distribution is shown in Fig. 8 for the plane with the highest power (plane 5). It should be noted that the results for this core will differ from that of a typical PWR core because all fuel assemblies contain fresh fuel and the moderator is not borated. This exaggerates the effect of moderation, especially at the core periphery. Nonetheless, it is interesting to note in Fig. 8 that there is a significant increase in the fuel temperature at the fuel pins adjacent to thermal neutron sources such as near the guide tubes and near the reflector region at the core periphery. In the complete temperature information that includes the sub-pin-level fuel temperature distributions, the azimuthal dependence of the clad temperature can also be examined so that local hot spots can be identified. This detailed intra-pin-level information would not be available in the current generation of coupled codes.

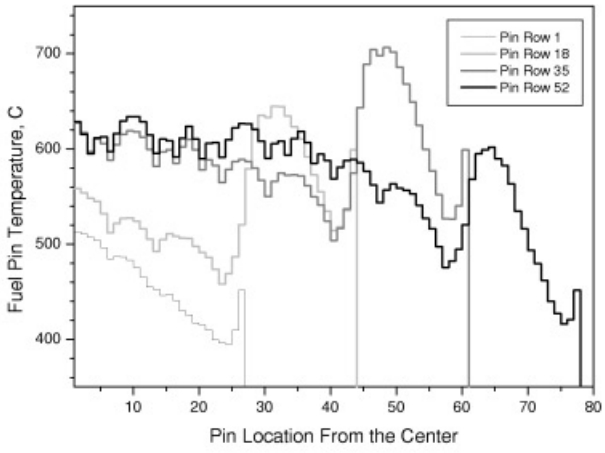

(a) along the assembly edge

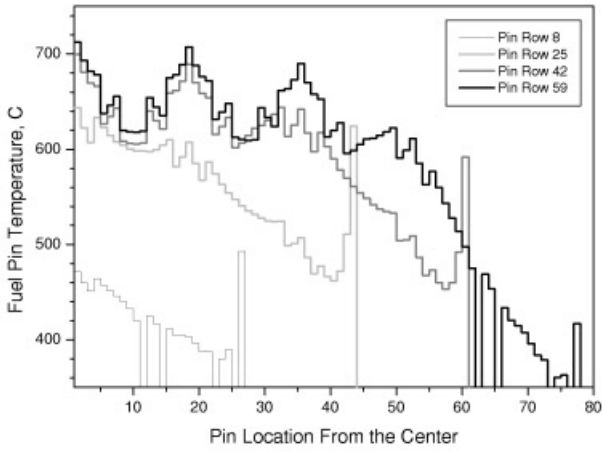

(b) along the line right below the assembly centerline

Fig. 8. Average fuel pin temperature for the plane with the highest power along selected rows of pins. Pin row 1 is for the bottom row in Fig. 7.

V. CONCLUSIONS AND FUTURE WORK

A methodology for integrating full-physics, high-fidelity reactor analysis was established and demonstrated in the work reported in this paper. It was shown that very detailed sub-pin-level power and temperature information can be obtained from the first-principles–based approach utilizing the high computing performance of a reasonably sized LINUX cluster. The half-day execution time is reasonable considering the accurate and detailed information provided by the NNR. Future applications of the NNR are anticipated for both LWRs and advanced reactors, though near-term emphasis will continue to be placed on LWRs. In addition to the capabilities described in this paper, transient analysis and depletion analysis capabilities have already been developed and will be validated using both numerical and experimental data.

For many applications to both PWRs and BWRs, the ability to predict thermal-hydraulic behavior under two-phase-boiling conditions is very important. A new boiling model has been implemented in the NNR CFD module, and an extensive testing and validation program has been initiated, with particular emphasis on the OECD/NRC benchmark exercise[40] for boiling behavior in BWR assemblies at prototypical temperature, pressure, and heat generation conditions. The extension of the boiling model to treat other expected flow regimes is in progress along with comparisons to the aforementioned rod bundle experiments.[36] An initial application of the newly developed BWR version of the NNR is currently in progress. In this program the NNR will be used to identify local thermal-hydraulic conditions under BWR operating conditions that will help explain the development of so-called tenacious crud, which may be responsible for some observed fuel failures.

The coupled code algorithms and methodology developed initially for LWRs appear easily extendible to other reactor types. For some such applications, further methods development and code validation will be necessary, as has been done for BWR applications. For applications such as gas-cooled reactors, analytical techniques are currently available, and programs are under

way for higher-fidelity representation. Using the same modular approach of the NNR, one can easily envision coupling neutronics, thermal hydraulics, and fuel performance in a robust analysis environment. With the importance of demonstrating economic operations and meeting safety requirements and the limitation of extensive experimental facilities, it is very likely that the nuclear community will move in the direction of simulation-based design, and high-fidelity, full-physics simulation capabilities such as the NNR will play an increasingly important role.

ACKNOWLEDGMENTS

This work was supported by the I-NERI program jointly funded by the Ministry of Science and Technology of Korea and the DOE. Additional activities related to the BWR version of the NNR were supported by the DOE.

REFERENCES

1. D. P. WEBER, H. G. JOO, T. J. DOWNAR, and C. H. KIM, "Integrated 3-D Simulation of Neutronic, Thermal-Hydraulic and Thermo-Mechanical Phenomena," presented at 10th Int. Topl. Mtg. Nuclear Reactor Thermal Hydraulics (NURETH-10), Seoul, Korea, October 5–9, 2003.

2. D. P. WEBER, T. SOFU, P. A. PFEIFFER, W. S. YANG, T. A. TAIWO, H. G. JOO, J. Y. CHO, K. S. KIM, T. H. CHUN, T. J. DOWNAR, J. W. THOMAS, Z. ZHONG, C. H. KIM, and B. S. HAN, "The Numerical Nuclear Reactor for High Fidelity Integrated Simulation of Neutronic, Thermal-Hydraulic and Thermo Mechanical Phenomena—Project Overview," *Proc. Physics of Fuel Cycles and Advanced Nuclear Systems: Global Developments (PHYSOR-2004)*, Chicago, Illinois, April 25–29, 2004, American Nuclear Society (2004) (CD-ROM).

3. T. SOFU, D. P. WEBER, T. H. CHUN, H. G. JOO, J. W. THOMAS, Z. ZHONG, and T. J. DOWNAR, "Development of a Comprehensive Modeling Capability based on Rigorous Treatment of Multi-Physics Phenomena Influencing Reactor Core Design," *Proc. Int. Congress on Advances in Nuclear Power Plants (ICAPP'04)*, Pittsburgh, Pennsylvania, June 13–17, 2004, American Nuclear Society (2004) (CD-ROM).

4. D. P. WEBER, T. SOFU, P. PFEIFFER, W. S. YANG, K. S. KIM. T. H. CHUN, T. DOWNAR, J. THOMAS, Z. ZHONG, H. G. JOO, and C. H. KIM, "The Numerical Nuclear Reactor—A High Fidelity, Integrated Neutronic, Thermal-Hydraulic and Thermo-Mechanical Code," presented at Int. Topl. Mtg. Mathematics and Computation, Supercomputing, Reactor Physics and Nuclear and Biological Applications, Avignon France, September 12–15, 2005.

5. H. G. JOO, J. Y. CHO, K. S. KIM, C. C. LEE, and S. Q. ZEE, "Methods and Performance of a Three-Dimensional Whole-Core Transport Code DeCART," *Proc. Physics of Fuel Cycles and Advanced Nuclear Systems: Global Developments (PHYSOR-2004)*, Chicago, Illinois, April 25–29, 2004, American Nuclear Society (2004) (CD-ROM).

6. M. J. HALSALL, "CACTUS, A Characteristics Solution to the Neutron Transport Equations in Complicated Geometries," AEEW-R-1291, United Kingdom Atomic Energy Authority, Winfrith (1980).

7. T. M. SUTTON, "NODEX: A High Order NEM-Based Multigroup Nodal Code," *Proc. Topl. Mtg. Advances in Nuclear Engineering Computation and Radiation Shielding*, Santa Fe, New Mexico, April 9–13, 1989, Vol. 1, p. 38:1, American Nuclear Society (1989).

8. K. SMITH and J. D. RHODES, III, "Full-Core, 2-D, LWR Core Calculations with CASMO-4E," *Proc. PHYSOR2002*, Seoul, Korea, October 7–10, 2002, paper 13A-04 (2002) (CD-ROM).

9. J. Y. CHO, H. G. JOO, K. S. KIM, S. Q. ZEE, and M. H. CHANG, "Three-Dimensional Heterogeneous Whole Core Transport Calculation Employing Planar MOC Solution," *Trans. Am. Nucl. Soc.*, **87**, 234 (2002).

10. H. G. JOO, J. Y. CHO, H. Y. KIM, S. Q. ZEE, and M. H. CHANG, "Dynamic Implementation of the Equivalence Theory in the Heterogeneous Whole Core Transport Calculation," *Proc. PHYSOR2002*, Seoul, Korea, October 7–10, 2002, paper 13A-02 (2002) (CD-ROM).

11. H. FINNEMANN, F. BENNEWITZ, and M. R. WAGNER, "Interface Nodal Current Techniques for Multidimensional Reactor Calculations," *Atomkernenergie*, **30**, 123 (1977).

12. J. Y. CHO, H. G. JOO, K. S. KIM, and S. Q. ZEE, "Cell-Based CMFD Formulation for Acceleration of Whole-Core Method of Characteristics Calculations," *J. Kor. Nucl. Soc.*, **35**, 250 (2002).

13. J. Y. CHO and H. G. JOO, "Solution of the C5G7MOX Benchmark Three-Dimensional Extension Problems by the DeCART Direct Whole Core Calculation Code," *Prog. Nucl. Energy*, **48**, 456 (2006).

14. H. G. JOO, B. S. HAN, C. H. KIM, and K. S. KIM, "Implementation of Subgroup Method in Direct Whole Core Transport Calculation Involving Nonuniform Temperature Distribution," *Proc. Mathematics and Computation (M&C2005)*, Palais des Papes, Avignon, France, September 12–15, 2005 (2005) (CD-ROM).

15. J. J. STAMMLER, "HELIOS Methods," Studsvik Scanpower (2000).

16. H. J. SHIM, B. S. HAN, and C. H. KIM, "Numerical Experiment on Variance Biases and Monte Carlo Neutronics Analysis with Thermal Hydraulic Feedback," *Proc. Int. Conf. Supercomputing in Nuclear Application (SNA03)*, Paris, France, September 22–24, 2003, Paper 103 (2003) (CD-ROM).

17. "Physics of Plutonium Fuels, BWR MOX Benchmark, Specification and Results," Working Party on the Physics of

Plutonium Fuels and Innovative Fuel Cycles, Volume VII, Nuclear Energy Agency/Organization for Economic Cooperation and Development (Jan. 2003).

18. E. A. GOMIN et al., "The Use of the Codes from MCU Family for Calculations of VVER Type Reactors," *Proc. 10th Atomic Energy Research Int. Topl. Mtg.*, Moscow, Russia, September 18–22, 2000.

19. G. YADIGAROGLU, "Computational Fluid Dynamics for Nuclear Applications: From CFD to Multi-Scale CMFD," *Nucl. Eng. Des.*, **235**, 153 (2005).

20. E. BAGLIETTO and H. NINOKATA, "A Turbulence Model Study for Simulating Flow Inside Tight Lattice Rod Bundles," *Nucl. Eng. Des.*, **235**, 773 (2005).

21. B. E. LAUNDER and D. B. SPALDING, "The Numerical Computation of Turbulent Flows," *Comput. Methods Appl. Mech. Eng.*, **3**, 269 (1974).

22. F. S. LIEN, W. L. CHEN, and M. A. LESCHZINER, "Low-Reynolds-Number Eddy-Viscosity Modelling Based on Nonlinear Stress-Strain/Vorticity Relations," *Proc. 3rd Symp. Engineering Turbulence Modeling and Measurements*, Crete, Greece, 1996.

23. W. RODI, "Experience with Two-Layer Models Combining k-ε Model with a One-Equation Model Near the Wall," *AIAA 29th Aerospace Sciences Mtg.*, Reno, Nevada, January 7–10, 1991, AIAA-1991-216, American Institute of Aeronautics and Astronautics (1991).

24. C. G. SPEZIALE, "On Non-Linear k-l and k-ε Models of Turbulence," *J. Fluid Mech.*, **178**, 459 (1987).

25. H. K. MYONG and N. KASAGI, "Prediction of Anisotropy of the Near Wall Turbulence with an Anisotropic Low-Reynolds-Number k-ε Turbulence Model," *J. Fluids Eng.*, **112**, 521 (1990).

26. T. H. SHIH, J. ZHU, and J. L. LUMLEY, "A Realizable Reynolds Stress Algebraic Equation Model," NASA Technical Memo 105993, National Aeronautics and Space Administration (1993).

27. T. J. CRAFT, B. E. LAUNDER, and K. SUGAR, "Development and Application of a Cubic Eddy-Viscosity Model of Turbulence," *Int. J. Heat Fluid Flow*, **17**, 108 (1996).

28. V. YAKHOT and S. A. ORSZAG, "Renormalization Group Analysis of Turbulence—I: Basic Theory," *J. Sci. Comput.*, **1**, 1 (1992).

29. Y. S. CHEN and S. W. KIM, "Computation of Turbulent Flows Using an Extended k-ε Turbulence Closure Model," NASA CR-179204, National Aeronautics and Space Administration (1897).

30. B. E. LAUNDER, G. J. REECE, and W. RODI, "Progress in the Development of a Reynolds Stress Turbulence Model," *J. Fluid Mech.*, **68**, 537 (1975).

31. F. W. DITTUS and L. M. K. BOELTER, *Univ. of Calif. (Berkeley) Pub. Eng.*, **2**, 443 (1930).

32. T. SOFU, T. H. CHUN, and W. K. IN, "Evaluation of Turbulence Models for Flow and Heat Transfer in Fuel Rod Bundle Geometries," *Proc. Physics of Fuel Cycles and Advanced Nuclear Systems: Global Developments (PHYSOR-2004)*, Chicago, Illinois, April 25–29, 2004, American Nuclear Society (2004) (CD-ROM).

33. J. D. HOOPER and D. H. WOOD, "Fully Developed Rod Bundle Flow over a Large Range of Reynolds Numbers," *Nucl. Eng. Des.*, **83**, 31 (1984).

34. T. KRAUSS and L. MEYER, "Experimental Investigation of Turbulent Transport of Momentum and Energy in a Heated Rod Bundle," *Nucl. Eng. Des.*, **180**, 185 (1998).

35. W. K. IN, C. H. SHIN, D. S. OH, and T. H. CHUN, "CFD Simulation of the Turbulent Flow and Heat Transfer in a Bare Rod Bundle," *Proc. Int. Congress on Advances in Nuclear Power Plants (ICAPP'04)*, Pittsburgh, Pennsylvania, June 13–17, 2004, American Nuclear Society (2004) (CD-ROM).

36. A. TENTNER, S. LO, A. IOILEV, M. SAMIGULIN, and V. USTINENKO, "Computational Fluid Dynamics Modeling of Two-Phase Flow in a Boiling Water Reactor Fuel Assembly," presented at Int. Topl. Mtg. Mathematics and Computation, Supercomputing, Reactor Physics and Nuclear and Biological Applications, Avignon France, September 12–15, 2005.

37. J. W. THOMAS, H. C. LEE, T. J. DOWNAR, T. SOFU, D. P. WEBER, H. G. JOO, and J. Y. CHO, "The Coupling of the STAR-CD Software to a Whole-Core Neutron Transport Code DeCART for PWR Applications," presented at Int. Conf. Supercomputing in Nuclear Applications (SNA 2003), Paris, France, September 2003.

38. J. W. THOMAS, Z. ZHONG, T. SOFU, and T. J. DOWNAR, "Methodology for Coupling Computational Fluid Dynamics and Integral Transport Neutronics," *Proc. Physics of Fuel Cycles and Advanced Nuclear Systems: Global Developments (PHYSOR-2004)*, Chicago, Illinois, April 25–29, 2004, American Nuclear Society (2004) (CD-ROM).

39. D. P. WEBER, T. SOFU, W. S. YANG, T. DOWNAR, J. THOMAS, Z. ZHONG, and H. G. JOO, "Coupled Calculations Using the Numerical Nuclear Reactor for Integrated Simulation of Neutronic and Thermal-Hydraulic Phenomena," *Proc. Physics of Fuel Cycles and Advanced Nuclear Systems: Global Developments (PHYSOR-2004)*, Chicago, Illinois, April 25–29, 2004, American Nuclear Society (2004) (CD-ROM).

40. G. G. BARTOLEMEI and V. M. CHANTURIYA, "Experimental Study of True Void Fraction When Boiling Subcooled Water in Vertical Tubes," *Thermal Eng.*, **14**, 123 (1967).